

frequency of the climate model, C_T the ocean's thermal overturning time, and C_L the ice cap's relaxation time. There are at least two ways to include external forcing in Eq. 4: with an additive term of the form $F \cos \omega_0 t$, which introduces the possibility of resonance when $\omega_0 \rightarrow \Omega$, and/or with a time-varying parameter (parametric excitation), assuming that Ω changes with the dimension of the ice sheet (21) through C_L , which is proportional to a critical dimension of the ice sheet (22).

If C_L is of the form $C_L(1 + \Delta C_L/C_L \cos \omega t)$ where $\Delta C_L \ll C_L$ and ω is the modulating frequency, Eq. 4 becomes

$$d^2L/dt^2 + \Omega^2 [1 + 2(\Delta\Omega/\Omega)\cos\omega t] L = 0 \quad (5)$$

which is the Mathieu equation (23), whose periodic solutions are frequency-modulated sinusoids (24) of the form

$$L \sim A \sin[\Omega t + (\Delta\Omega/\omega)\sin \omega t + \phi] \quad (6)$$

where A and ϕ are integration constants. The solution to Eq. 6 is of the same form as each of the terms of Eq. 3 used to simulate the $\delta^{18}\text{O}$ records. Nonlinear forms of Eq. 5 are known to develop instabilities, bifurcations, and period-doubling cascades into chaos (25).

References and Notes

1. M. Milankovitch, *Canon of Insolation and the Ice-Age Problem*, Royal Serbian Academy Spec. Pub., vol. 132 (Israel Program for Scientific Translations, Jerusalem, 1969).
2. J. D. Hays, J. Imbrie, N. J. Shackleton, *Science* **194**, 1121 (1976).
3. A. Berger and M. F. Loutre, *Quat. Sci. Rev.* **10**, 297 (1991); A. Berger, *Numerical Values of the Elements of the Earth's Orbit from 5,000,000 YBP to 1,000,000 YAP*, Contribution No. 35, Universite Catholique de Louvain, B-1348 Louvain, Belgium (1978).
4. J. Imbrie et al., in *Milankovitch and Climate*, A. L. Berger et al., Eds. (Reidel, Hingham, MA, 1984), pp. 269–305.
5. In order of decreasing spectral amplitude, the main periods in the trigonometric expansion of Earth's orbital eccentricity are, approximately, 413, 95, 125, and 100 ky. The 95 and 413 ky spectral peak amplitudes are nearly equal and about twice as strong as the 125 ky amplitude and four times stronger than the 100 ky amplitude (3).
6. J. Imbrie and J. Z. Imbrie, *Science* **207**, 943 (1980).
7. M. E. Raymo, *Paleoceanography* **12**, 577 (1997).
8. W. H. Berger, M. K. Yasuda, T. Bickert, G. Wefer, T. Takayama, *Geology* **22**, 463 (1994); W. H. Berger, T. Bickert, H. Schmidt, G. Wefer, *Proc. Ocean Drill. Program Part B Sci. Results* **130**, 381 (1993).
9. B. P. Lathi, *Modern Digital and Analog Communication Systems* (Oxford Univ. Press, New York, 1998).
10. The sidebands of a carrier of frequency f_c frequency modulated by a signal of frequency f_m are located at $f_c \pm n f_m$, $n = 1, 2, 3, \dots$. See, for instance, A. Hund, *Frequency Modulation* (McGraw-Hill, New York, 1942).
11. Frequency modulation of the weaker 125 ky eccentricity component essentially reinforces the 95 ky peak and its sidebands, since $1/95 \sim 1/413 \sim 1/125$. The contribution of the much weaker 100 ky component is noticeable only in some records (Fig. 4A).
12. D. G. Martinson et al., *Quat. Res.* **27**, 1 (1987).
13. Age models for the $\delta^{18}\text{O}$ data used in this study are as follows: Site 849 and Site 846 tuning procedures are described in Mix et al. (19). For the construction of the untuned records, the following anchor points between depth (revised composite depth in meters, or rmc) and age were used. Site 846: 0.0 rmc = 0.00 thousand years

before the present (ky B.P.); 65.4 rmc = 1810 ky B.P. Site 849: 0.0 rmc = 0.0 ky B.P.; 50.0 rmc = 1800 ky B.P.; 153.8 rmc = 5 My B.P. (A. Mix, personal communication). The untuned time scale was then constructed by linear interpolation. Both tuned and raw records are available through anonymous ftp (<ftp://oce.orst.edu/DATA/mix>). Site 806: The age model for the tuned record of Site 806 is from (8). Site 677: Tuned and depth-dependent data were obtained from the Delphi project Web site (<http://delphi.esc.cam.ac.uk/>). See also N. J. Shackleton, A. Berger, and W. R. Peltier [*Trans. R. Soc. Edinburgh Earth Sci.* **81**, 251 (1990)]. To construct the untuned record, two anchor points at 0 ky B.P. and at 1200 ky B.P. were transferred from the tuned age model. The untuned time scale was then constructed by linear interpolation.

14. R. A. Muller and G. J. MacDonald, *Science* **277**, 215 (1997).
15. The frequency resolution of a 600 ky window is at best $1/600 \text{ ky}^{-1}$, or 0.00167 cycles/ky, so that the spectrum entirely washes out the gap between the eccentricity's 95-ky carrier and the important 107-ky sideband, separated by a $1/826 = 0.00121$ cycles/ky interval, and barely resolves sidebands produced by the 413-ky modulation, separated by multiple integers of 0.00242 cycles/ky. A possible reason for the presence of a strong 100-ky peak in the short window spectra is found in the spectrogram of Fig. 1B, which shows that the highest power in the eccentricity band is associated with a transient event about 400 ka (well within the 0 to 600 ky window), which lasted for about 100 ky and had most of its power between 90 and 110 ky. Low spectral resolution of this transient event can certainly contribute to make the 100-ky peak (14) as prominent as shown in Fig. 3C.
16. Even in tuned spectra, results show [J. Park and K. A. Maasch, *J. Geophys. Res.* **98**, 447 (1993)] that the presence of 95 ky and 125 ky peaks in $\delta^{18}\text{O}$ records is unlikely to be an artifact of time scaling techniques, because different time series treated with different tuning schemes contain the two eccentricity peaks prominently, even for times before 1 Ma.
17. Increase in the modulation index ϵ increases the number of sidebands and hence the bandwidth. Its increase

also increases the power of the sidebands relative to the carrier's (Fig. 4).

18. This is because $\sin[\omega_c t + \epsilon \sin \omega_m t + \epsilon' \sin \omega_m t] \neq \sin[\omega_c t + \epsilon \sin \omega_m t] + \sin[\omega_c t + \epsilon' \sin \omega_m t]$. An interesting point is then that Eq. 3 represents a climate response that is both linear and nonlinear, since it allows for the linear superposition of the spectra of each individual modulated carrier and its sidebands, while the FM process acting on each carrier is itself nonlinear. In fact, having more than one modulating frequency creates an infinite number of combination tones (this distinguishes FM from AM, or amplitude modulation), and so Eq. 3 predicts that the spectral peak at 107 ky is strong because it is both a sideband of the 95-ky carrier modulated by the 826-ky subharmonic and a nonlinearly produced combination tone, which probably explains why it appears to have its own sidebands (Fig. 4).
19. A. C. Mix et al., *Proc. Ocean Drill. Program Part B Sci. Results* **138**, 371 (1995); A. C. Mix, J. Le, N. J. Shackleton, *ibid.*, p. 839.
20. M. Ghil and S. Childress, *Topics in Geophysical Fluid Dynamics: Atmospheric Dynamics, Dynamo Theory and Climate Dynamics* (Springer-Verlag, Berlin, 1987).
21. The capacitor of a resonating circuit is analogous to the ice sheet in that it stores energy in proportion to its area. An FM signal is created, for instance, by sinusoidally varying the circuit's capacitance.
22. E. Kallén, C. Crafoord, M. Ghil, *J. Atmos. Dyn.* **36**, 2292 (1980).
23. Mathieu's equation is a particular case of Hill's equation, arising in many practical applications and in the theory of astronomical perturbations.
24. L. A. Pipes and L. R. Harvill, *Applied Mathematics for Engineers and Physicists* (McGraw-Hill, New York, 1970).
25. T. Mulin, Ed., *The Nature of Chaos* (Clarendon, Oxford, 1993).
26. L. Hinnov, A. Mix, F. Schmieder, J. Park, and B. Bills provided useful comments, data, and continuous encouragement, for which I will always be grateful. Reaction to a critical anonymous review made this paper publishable. The research was supported in part by grants from NSF, U.S. Department of Energy, and the University of North Carolina Research Council.

27 January 1999; accepted 18 June 1999

The Role of Sub-Milankovitch Climatic Forcing in the Initiation of the Northern Hemisphere Glaciation

K. J. Willis,^{1*} A. Kleczkowski,^{2†} K. M. Briggs,² C. A. Gilligan²

Mechanisms responsible for the initiation of major glaciation in the Northern Hemisphere at about 2.75 million years ago are poorly understood. A laminated terrestrial sequence from Pula maar, Hungary, containing about 320,000 years in annual layers between 3.05 and 2.60 million years ago, provides a detailed record of rates of climatic change across this dramatic transition. An analysis of the record implies that climatic variations at sub-Milankovitch frequencies (less than or equal to 15,000 years) were an important driving force during this transitional interval and that, as the threshold was approached, these increased in frequency and amplitude, possibly providing the final trigger for the amplification of Northern Hemisphere ice sheets.

The late Pliocene was a time of major climatic cooling resulting in the growth of large terrestrial ice sheets and the onset of Northern Hemisphere glaciation (NHG) at ~2.75 million years ago (Ma). What triggered this dramatic period of global environmental change has been uncertain (1). Suggestions include climatic change

associated with changing continental positions and altered deep ocean circulation (2, 3), a long-term decline in atmospheric CO₂ levels resulting in greenhouse cooling (4), climate change associated with tectonic uplift (5), and decreased rates of sea-floor spreading (6). It has also been suggested that the onset of NHG was

REPORTS

at least partially controlled by long-term periodic variations in incoming solar radiation (4, 7); calculations indicate that climatic variations associated with orbital forcing may have determined the timing of glacial episodes (1) and that incremental increases in obliquity between ~3.1 and 2.5 Ma provided the final trigger for amplification and expansion of the Northern Hemisphere ice sheets (3). Here, we present results from a high-resolution terrestrial record that demonstrates that, in addition to climate change at orbital frequencies, substantial variations were also occurring at much higher frequencies ($\leq 15,000$ years) (sub-Milankovitch cycles) during this critical period of global environmental change.

The 45-m terrestrial sequence from Pula maar crater lake in Hungary represents ~320,000 years of accumulation between 3.05 and 2.60 Ma (8). The sediments are composed of alternating light and dark layers; a pair of layers represents a single year's deposition. The light layers are a calcium carbonate matrix and represent summer accumulation, whereas the dark layers contain the algae *Botryococcus braunii* and represent deposition during the winter months (8–10). Measurements of the laminations at set intervals down the core indicate that an accumulation rate of 80 ± 10 years/cm was relatively constant throughout the sequence. K/Ar dating, in conjunction with magnetic polarity reversal data, indicates that the sequence is located in the Gauss epoch (polarity chron C2An.1n), dated between 3.05 and 2.60 Ma. This allows the placement of the boundaries with an accuracy of $\pm 40,000$ years while maintaining an accurate time scale within the record.

The core was subsampled at intervals of ~2500 years throughout and analyzed for fossil pollen. Terrestrial vegetation dynamics are clearly represented in the record by cycles alternating between subtropical-temperate forest and boreal forest (8). Increases in boreal pollen percentages correlate with decreases in global temperature demonstrated in the marine oxygen isotope record [$\delta^{18}\text{O}$ from Ocean Drilling Program (ODP) site 846 (11)] for this time period (Fig. 1).

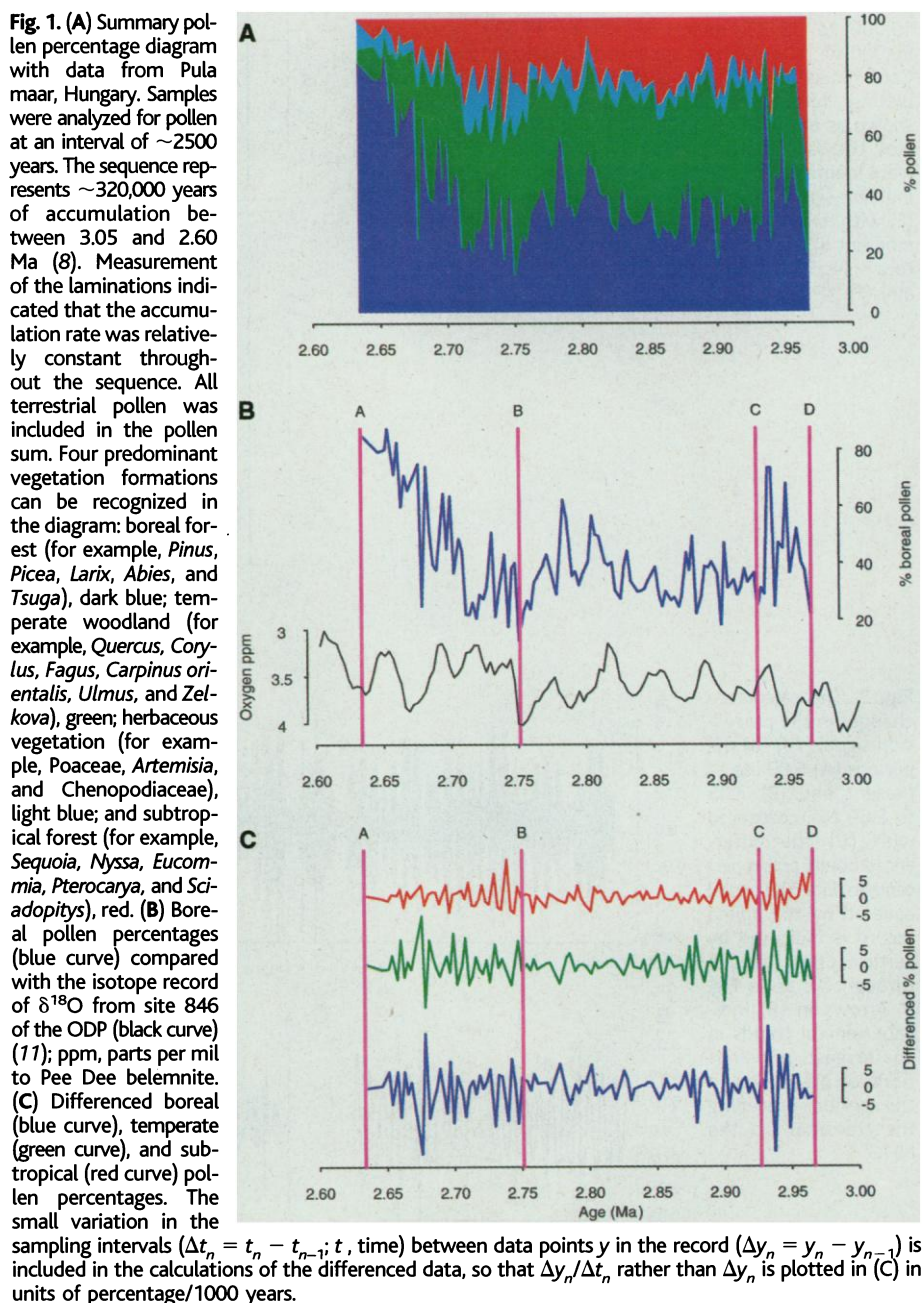
At the broadest scale, the record shows a long-term decline in subtropical-temperate forest and an increase in boreal forest (Fig. 1A). Superimposed on this trend is a transition between ~2.75 and 2.64 Ma, represented by the rapid increase in boreal forest, a dramatic decline in temperate tree taxa, and the

final demise of subtropical types from the lake area (Fig. 1B, lines A and B). The age of this transition relates to a time when there was a substantial growth of large terrestrial ice sheets and an intensification of the NHG (7, 11, 12).

To analyze the character of the vegetation dynamics across this NHG transition, we calculated the rates of change of boreal pollen percentage by taking the first differences (Figs. 1C and 2A) [a procedure similar to that used in (13)]. Spectral analysis of these differenced data revealed strong climatic variability at sub-Milankovitch time scales ($\leq 15,000$ years) throughout the whole sequence (Fig. 2C, lines A through D). However, the periodicity is not distributed evenly, and there is a sharp transi-

tion from low-amplitude low-frequency cycles before 2.75 Ma to high-amplitude high-frequency oscillations from 2.75 to 2.64 Ma. Thus, between 2.93 and 2.75 Ma (Fig. 2C, lines C and B), the spectral power is concentrated at periods of 15,000 years in addition to a period of 23,000 years (8) (Fig. 2, C and D). This is in contrast to the section of the core between ~2.75 and 2.64 Ma (Fig. 2E, lines A and B), which is dominated by oscillations with periods of $< 10,000$ years (Fig. 2F). The results from this core imply that, as the NHG transition was approached, climatic variability at sub-Milankovitch time scales became more pronounced and more frequent.

Variations at these time scales are absent from the calculated orbital insolation (14).



¹Godwin Institute for Quaternary Research, Cambridge CB2 3EJ, UK. ²Department of Plant Sciences, University of Cambridge, Cambridge CB2 3EA, UK.

*Present address: School of Geography, University of Oxford, Oxford OX1 3TB, UK.

†To whom correspondence should be addressed. E-mail: a.kleczkowski@kings.cam.ac.uk

REPORTS

Fig. 2. Spectral analysis of the differenced boreal pollen percentage data. The differencing of the data enhances the detectability of the sub-Milankovitch cycles in the spectra otherwise dominated by low-frequency components (8). (A and B) The whole record, (C and D) the record between 2.93 and 2.75 Ma, and (E and F) the record between 2.75 and 2.64 Ma. The pollen data shown in Fig. 1B were interpolated to the equal time step of 3000 years (resulting in the time series of the same length as the original), differenced [(A), (C), and (E)], and subsequently analyzed with the Burg [maximum entropy (17)] method, which involves fitting an autoregressive (AR) process to the data and estimating the power spectrum of this process [(B), (D), and (F)]. Other interpolation methods [including smoothing] and spectral analysis techniques [including Blackman-Tukey, periodogram, maximum likelihood, least squares, and Lomb (17)] were also tested, but these did not substantially affect the principal inferences. The order of the AR processes was determined as the minimal order for which the spectrum was consistent with other methods, notably the Lomb method (which does not require interpolation). Approximate Milankovitch bands for periods of 19,000 to 23,000 years, 38,000 to 44,000 years, and 90,000 to 140,000 years are shown in spectral plots (gray). Confidence limits for the spectra were calculated by simulating white noise, and 0.025, 0.5, and 0.975 quantiles are shown as dashed lines in (B), (D), and (F). In each spectral plot, the oscillations corresponding to a leading frequency were identified (marked by a triangle), and the corresponding sine signals are shown for comparison in (A), (C), and (E) with an arbitrary phase. A combination of the cyclicity inherent in the sequence and the sampling procedure leads to a selection of discrete peaks at high frequencies in (B) and (F).

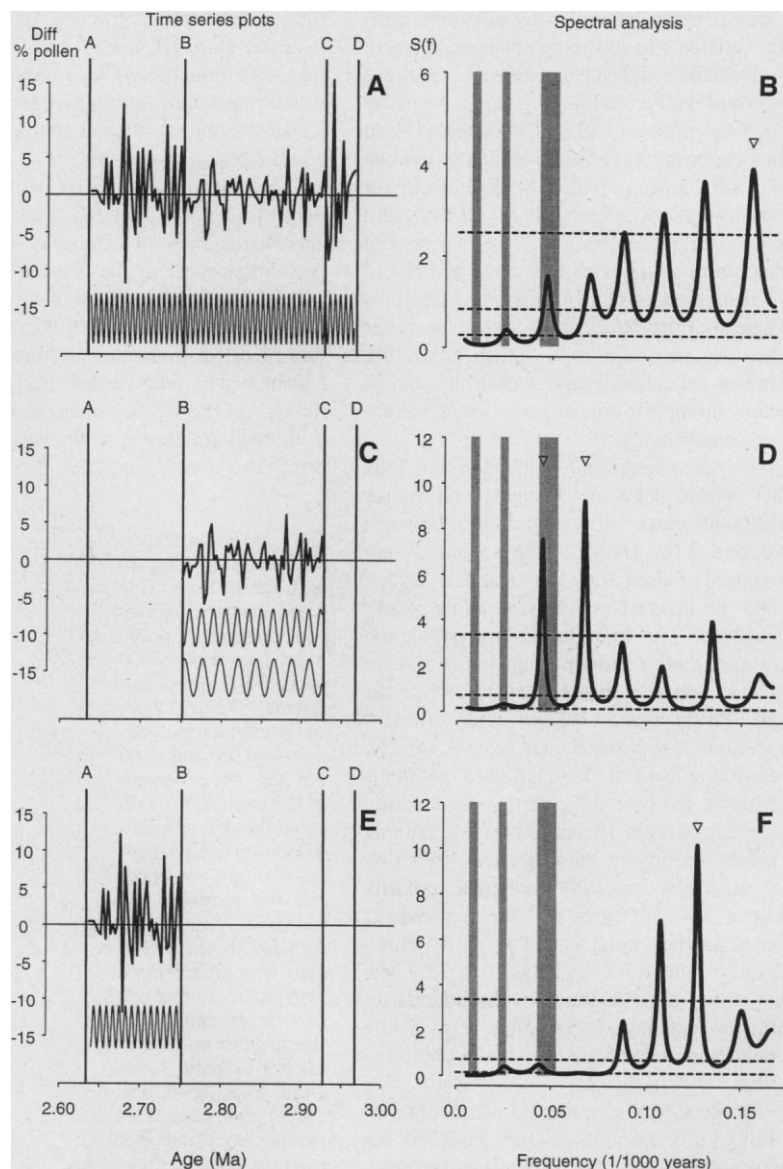
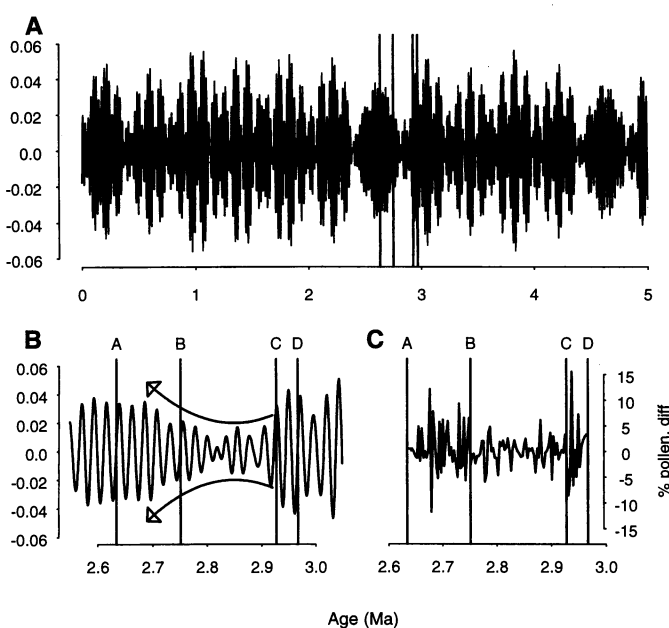


Fig. 3. The calculated changes in the precession signal (14) for the periods (A) 5.00 Ma to present and (B) 3.05 to 2.60 Ma, compared with (C) the differenced boreal pollen percentage data. The period covered by the pollen record is indicated by vertical lines (lines A through D), as in Fig. 1. Arrows in (B) indicate general trends in an increase of variations in the period preceding the transition to the NHG.



This has led to the conclusion (15) that, in the Pleistocene, the climatic variability at sub-Milankovitch time scales is at least partly nonlinearly transferred from the precession band (19,000 to 23,000 years). To explore the possibility for a similar mechanism in the late Pliocene, we compared the pollen record with the calculated precession signal between 3.05 and 2.60 Ma. The orbital forcing is characterized by three distinct periods: A period of low-amplitude oscillations (2.93 to 2.75 Ma) (Fig. 3, A and B, lines B and C) is framed by two periods of high-amplitude cycles (Fig. 3B, lines A and B and C and D). Qualitatively, the same behavior is thus observed in the differenced signal of the boreal pollen percentage (Fig. 3C), suggesting that the dynamics of the terrestrial vegetation at sub-Milankovitch frequencies in the late Pliocene may be linked to the precession signal. However, the Pula maar sequence is responding at much higher frequencies ($\leq 15,000$ years as

opposed to 19,000 to 23,000 years in the insolation record), indicating a more complicated relation (15, 16).

Our results demonstrate that embedded within the long-term climatic changes were much finer scale variations at sub-Milankovitch time scales (Fig. 2). We therefore propose that, in addition to the climatic changes associated with the linear response to the orbital forcing, a nonlinear response at sub-Milankovitch frequencies may have been responsible for the initiation of the NHG. Perhaps an incremental increase in amplitude and frequency of these sub-Milankovitch oscillations across the transition resulted in a shortening of the length of time between subsequent cold stages. This would have reduced the time for climatic "recovery" between each cycle, thereby providing a mechanism for the buildup of large terrestrial ice

sheets. Thus, a combination of factors at different time scales within a nonlinear framework may be responsible for the changes leading to the NHG.

References and Notes

1. L. J. Lourens and F. J. Hilgen, *Quat. Int.* **40**, 43 (1997).
2. M. E. Raymo, D. Hodell, E. Jansen, *Paleoceanography* **7**, 645 (1992).
3. G. H. Haug and R. Tiedemann, *Nature* **393**, 673 (1998).
4. X. S. Li *et al.*, *Geophys. Res. Lett.* **25**, 915 (1998).
5. W. F. Ruddimann and J. E. Kutzbach, *J. Geophys. Res.* **94**, 18409 (1989).
6. M. E. Raymo, W. F. Ruddimann, P. N. Froelich, *Geology* **16**, 649 (1988).
7. M. A. Maslin, X. S. Li, M. F. Loutre, A. Berger, *Quat. Sci. Rev.* **17**, 411 (1998).
8. K. J. Willis, A. Kleczkowski, S. J. Crowhurst, *Nature* **397**, 685 (1999).
9. C. Ravasz, *Annu. Rep. Hung. State Geol. Inst.* 1974 (1974), p. 221.
10. M. Hajós, *Annu. Rep. Hung. State Geol. Inst.* 1988 (1988), p. 5.

11. N. J. Shackleton, M. A. Hall, D. Pate, in *Proceedings of the Ocean Drilling Program, Scientific Results*, N. G. Pisias, T. R. Janecek, A. Palmer-Julson, T. H. van Andel, Eds. (Ocean Drilling Program, College Station, TX, 1995), vol. 138, pp. 337-355.
12. M. A. Maslin, G. H. Haug, M. Sarnthein, R. Tiedemann, *Geol. Rundsch.* **85**, 452 (1996).
13. C. Kukla, *Boreas* **1**, 63 (1972).
14. J. Laskar, F. Joutel, F. Boudin, *Astron. Astrophys.* **270**, 522 (1993).
15. T. K. Hagelberg, G. Bond, P. deMenocal, *Paleoceanography* **9**, 545 (1994).
16. A. Berger and M. F. Loutre, *Science* **278**, 1476 (1997).
17. D. B. Percival and A. T. Walden, *Spectral Analysis for Physical Applications* (Cambridge Univ. Press, Cambridge, 1993).
18. This work was supported by a Royal Society University Research Fellowship (K.J.W.), a King's College Senior Research Fellowship (A.K.), Biotechnology and Biological Sciences Research Council (K.M.B. and C.A.G.), a Royal Society Leverhulme Trust Senior Research Fellowship (C.A.G.), and St. Hugh's College Oxford Higher Studies Fund (payment for color of Fig. 1), which we gratefully acknowledge.

4 January 1999; accepted 7 June 1999

Superradiant Rayleigh Scattering from a Bose-Einstein Condensate

S. Inouye,* A. P. Chikkatur, D. M. Stamper-Kurn, J. Stenger, D. E. Pritchard, W. Ketterle

Rayleigh scattering off a Bose-Einstein condensate was studied. Exposing an elongated condensate to a single off-resonant laser beam resulted in the observation of highly directional scattering of light and atoms. This collective light scattering is caused by the coherent center-of-mass motion of the atoms in the condensate. A directional beam of recoiling atoms was built up by matter wave amplification.

Rayleigh scattering, the scattering of a photon off an atom, is the most elementary process involving atoms and light. It is responsible for the index of refraction of gases, the blue sky, and resonance fluorescence. This process can be divided into absorption of a photon and subsequent spontaneous emission. Photon scattering imparts a recoil momentum to the atom. Because of the random nature of spontaneous emission, the direction of the recoil is random, leading to momentum diffusion and heating of the atomic motion.

With the realization of Bose-Einstein condensation (BEC) (1), it is now possible to study the interactions of coherent light with an ensemble of atoms in a single quantum state. The high degree of spatial and temporal coherence of a condensate was confirmed in several experiments (2, 3). This raises the important question of whether the coherent

external motion of the atoms can alter the interactions between atoms and light. Here we show that the long coherence time of a Bose-Einstein condensate introduces strong correlations between successive Rayleigh scattering events. The scattering of photons leaves an imprint in the condensate in the form of long-lived excitations that provide a positive feedback and lead to directional Rayleigh scattering.

The gain mechanism for Rayleigh scattering from a condensate can be derived semi-classically. When a condensate of N_0 atoms is exposed to a laser beam with wave vector \mathbf{k}_0 and scatters a photon with wave vector \mathbf{k}_s , an atom [or quasi-particle, also called momentum side mode in (4)] with recoil momentum $\hbar\mathbf{K}_j = \hbar(\mathbf{k}_0 - \mathbf{k}_s)$, where \hbar is Planck's constant divided by 2π , is generated. Because light propagates at a velocity about 10 orders of magnitude greater than the atomic recoil velocity (3 cm/s for sodium), the recoiling atoms remain within the volume of the condensate long after the photons have left and affect subsequent scattering events. They interfere with the condensate at rest to form a

moving matter wave grating of wave vector \mathbf{K}_j , which diffracts the laser beam into the phase-matching direction $\mathbf{k}_j (= \mathbf{k}_0 - \mathbf{K}_j)$. This diffraction is a self-amplifying process because every diffracted photon creates another recoiling atom that increases the amplitude of the matter wave grating.

When N_j recoiling atoms with momentum $\hbar\mathbf{K}_j$ interfere with N_0 condensate atoms at rest, the density modulation comprises $N_{\text{mod}} = 2\sqrt{N_0N_j}$ atoms. The light scattered by these atoms interferes constructively in the phase-matching direction with a total power P of

$$P = \hbar\omega_j R \frac{N_{\text{mod}}^2}{4} \quad (1)$$

$$f_j = \frac{\sin^2\theta_j}{8\pi/3} \Omega_j \quad (2)$$

Here, R is the rate for single-atom Rayleigh scattering, which is proportional to the laser intensity, and ω is the frequency of the radiation. The angular term in Eq. 2 reflects the dipolar emission pattern with θ_j being the angle between the polarization of the incident light and the direction of emission. Because of the finite size of the sample, the phase-matching condition is fulfilled over the solid angle $\Omega_j \sim \lambda^2/A$, where A is the cross-sectional area of the condensate perpendicular to the direction of the light emission and λ is the optical wavelength. More rigorously, Ω_j is given by the usual phase-matching integral for superradiance in extended samples (5):

$$\Omega_j = \int d\Omega(\mathbf{k}) \left| \int \tilde{\rho}(\mathbf{r}) e^{i(\mathbf{k}_i - \mathbf{k}) \cdot \mathbf{r}} d\mathbf{r} \right|^2 \quad (3)$$

where $|\mathbf{k}| = |\mathbf{k}_i|$ and $\tilde{\rho}(\mathbf{r})$ is the normalized spatial density distribution in the condensate ($\int \tilde{\rho}(\mathbf{r}) d\mathbf{r} = 1$).

Because each scattered photon creates a

Department of Physics and Research Laboratory of Electronics, Massachusetts Institute of Technology, Cambridge, MA 02139, USA.

*To whom correspondence should be addressed. E-mail: sinouye@mit.edu